https://doi.org/10.5194/wes-2025-81
Preprint. Discussion started: 27 May 2025

eawe european academy of wind energy
Open Access WIND ENERGY SCIENCE DISCUSSIONS

Impact of Yaw–Induced Unsteady Aerodynamics on BEM Prediction Accuracy: CFD Analysis Based on the NREL Phase VI Wind Turbine

JiaHong Hu, Hui Yang, and JiaXin Yuan

College of Air Transportation, Shanghai University of Engineering Science, Shanghai 201620, China;

Correspondence: Hui Yang (08130002@sues.edu.cn)

Abstract.

Accurately predicting the aerodynamic loads on wind turbine blades under yawed inflow remains a major challenge due to the complexity of three–dimensional unsteady flow phenomena. This study combines high-fidelity computational fluid dynamics (CFD) simulations and NREL Phase VI experimental data with a newly proposed normalized absolute error metric to evaluate the prediction accuracy of the modified blade element momentum (BEM) method under yawed and non-yawed inflow conditions, thereby quantitatively assessing the differences between different yaw angles, inflow velocities, and spanwise blade positions.In addition, the CFD results are employed to analyze the potential flow mechanisms responsible for the deterioration of BEM prediction accuracy. The results show that while the BEM method maintains high accuracy under non–yawed attached flow conditions, its performance deteriorates significantly under flow separation and yawed inflow. At a yaw angle of 30 and an inflow velocity of $15\ \mathrm{m/s}$, the force coefficient (C_n) prediction error at the blade root increases to 48.6%, exceeding the non–yawed case by more than 20%. Flow field analyses reveal that yawed inflow intensifies vortex interactions on the leeward side and induces strong spanwise vortex bands driven by Coriolis forces, causing stall regions to propagate from blade tip to root. These phenomena lead to severe local aerodynamic load fluctuations that are not captured by conventional BEM formulations based on steady–state assumptions. This study quantitatively demonstrates the degradation of BEM prediction accuracy under yawed conditions and systematically reveals the direct impact of stall vortex evolution on aerodynamic load variations. These findings provide physical insights for the development of next–generation aerodynamic models incorporating three–dimensional unsteady flow corrections.

1 Introduction

Accurate prediction of aerodynamic loads on wind turbine blades is essential for ensuring power output, efficiency, and structural integrity (Dai et al., 2024). Blade aerodynamics are influenced by various factors, including inflow velocity variations, wind direction changes, and turbulence intensity. Among these, yawed inflow–in which the wind direction deviates from the rotor plane–introduces additional three–dimensional unsteady flow phenomena. These significantly complicate the aerodynamic environment. The resulting challenges in aerodynamic load prediction can lead to non–uniform pressure distributions and unsteady loading, which under extreme conditions may cause blade structural damage or even failure (Zhang et al., 2024).

https://doi.org/10.5194/wes-2025-81
Preprint. Discussion started: 27 May 2025

eawe european academy of wind energy
Open Access WIND ENERGY SCIENCE DISCUSSIONS

Therefore, achieving accurate aerodynamic load prediction under complex yawed flow conditions remains a critical scientific problem in modern wind energy research.

Various approaches have been developed to predict the aerodynamic performance of wind turbine blades, including blade element momentum (BEM) theory, vortex wake methods, wind tunnel experiments, and computational fluid dynamics (CFD) simulations (Ji et al., 2022). Among them, the BEM method has become the most widely used in engineering applications due to its computational efficiency and ease of integration with optimization frameworks such as genetic algorithms and machine learning (Ram et al., 2019; Chehouri et al., 2015; Özkan and Genç, 2023). It is commonly used for model analysis (Mancini et al., 2023; Selvatici and Stevens, 2025),load prediction (Elgammi et al., 2020; Selvatici and Stevens, 2025), power estimation (Amoretti et al., 2023; Malik and Bak, 2025), fatigue analysis (Liu et al., 2020; Potentier et al., 2022), and blade shape optimization (Xu et al., 2023b, a).

To extend the applicability of the blade element momentum (BEM) theory to more complex aerodynamic conditions—including dynamic stall, 3D rotational effects, and yawed inflow—early studies have introduced various empirical correction models. Representative examples include Glauert's yaw correction (GIanert, 1935), the Beddoes–Leishman dynamic stall model (Leishman and Beddoes, 1986), and Du's stall delay model based on 3D boundary layer characteristics (Du and Selig, 1998). These corrections have been widely incorporated into commercial aerodynamic analysis tools such as GH Bladed and OpenFAST (Damiani et al., 2016), and have provided valuable support for engineering applications.In recent years, research attention has gradually shifted toward physics-based approaches that aim to more accurately capture critical unsteady aerodynamic features. For example, Bangga et al. (2020) proposed a second-order dynamic stall model capable of reproducing higher-order vortex-shedding harmonics across different airfoils and flow conditions. Notably, this model eliminates the need for airfoil-specific parameter calibration while maintaining excellent agreement with experimental dynamic polars.

However, the BEM framework remains fundamentally limited by its reliance on two–dimensional, steady–state airfoil data. This assumption prevents the model from capturing key unsteady aerodynamic features such as vortex shedding, rotational augmentation, and stall delay–particularly under yawed inflow, where complex three–dimensional vortex interactions dominate.

CFD simulations, by directly solving the Navier–Stokes equations, offer a more accurate and detailed alternative. They have been proven effective in analyzing wake evolution, turbulence interactions, and unsteady stall dynamics. Nonetheless, their high computational cost and strict requirements on mesh quality and solver stability continue to limit their widespread use in practical wind farm design (Monteiro et al., 2009). Recent studies have attempted to combine the strengths of BEM and CFD. For example, Yang et al. (Yang et al., 2014) used CFD to refine airfoil characteristics within BEM codes based on the MEXICO turbine, while Laalej et al. (Laalej et al., 2022) developed a hybrid BEM–CFD model for improved load and power prediction. However, these works mainly focus on correcting two–dimensional inputs or idealized flow scenarios. To date, there remains a lack of systematic investigations into the accuracy of BEM under highly three–dimensional yawed inflow conditions, and the physical flow mechanisms driving its prediction errors are still poorly understood.

To address this gap, the present study systematically investigates the aerodynamic prediction accuracy of a corrected BEM method under both yawed and non–yawed inflow conditions. The NREL Phase VI wind turbine is selected as the benchmark

https://doi.org/10.5194/wes-2025-81
Preprint. Discussion started: 27 May 2025

case due to the availability of high–quality experimental data. High–fidelity CFD simulations, validated against the experimental results, are employed to provide detailed flow field information and reference aerodynamic loads. The evolution of prediction errors under different conditions is quantified by comparing the BEM and CFD predictions across a range of inflow velocities and yaw angles. Additionally, key flow structures near the blade root, mid–span, and tip are analyzed. Furthermore, the CFD flow field is used to identify the unsteady aerodynamic phenomena–such as spanwise vortex bands and dynamic stall–that contribute to the degradation of BEM performance under yawed inflow.

This study makes the following contributions:

- It provides a systematic evaluation of BEM prediction accuracy under both yawed and non–yawed inflow conditions using the NREL Phase VI wind turbine, quantifying how prediction errors evolve with yaw angle, inflow velocity, and blade spanwise location.

- It leverages validated CFD simulations to reveal the flow–physics mechanisms–such as spanwise vortex development, leading– and trailing–edge vortex interactions, and stall progression–that contribute to the degradation of BEM accuracy under yaw–induced unsteady conditions.

- It offers new insights into the limitations of conventional BEM assumptions under complex flow environments and provides a physics–based reference framework for the development of next–generation BEM models incorporating three–dimensional unsteady corrections.

2 Materials and Methods

The rotor of the Phase VI wind turbine consists of two twisted, tapered blades based on the S809 airfoil profile, each with a length of $5.029\ \mathrm{m}$. The detailed structure and blade parameters are shown in Figure 1. The Phase VI experiment, conducted by the National Renewable Energy Laboratory (NREL) (Simms et al., 2001), is regarded as one of the most significant and comprehensive aerodynamic experiments for wind turbines to date. This study focuses on analyzing the aerodynamic performance of the rotor under different yaw angles and inflow velocities at the rated rotational speed of $72\ \mathrm{rpm}$, aiming to investigate the effects of flow separation and rotational augmentation on aerodynamic prediction. Prior to the simulation, appropriate configurations were established for the different computational methods, and initial conditions were carefully preprocessed.

2.1 BEM Method

For the corrected BEM method, this study employs the FAST code developed by NREL, with a particular focus on its aerodynamic module, AeroDyn. The module utilizes the Unsteady Aerodynamics Module (UAM) for the analysis of two–dimensional airfoils, accounting for unsteady aerodynamic effects under additional flow conditions as well as dynamic stall, thereby reducing the errors associated with using static airfoil aerodynamic parameters. The UAM primarily adopts a variant of the widely used Beddoes–Leishman (B–L) semi–empirical model for unsteady aerodynamic and dynamic stall applications. When calculating the dynamic stall characteristics of the S809 airfoil using this module, the detailed input parameters are listed in Table 1.

https://doi.org/10.5194/wes-2025-81
Preprint. Discussion started: 27 May 2025

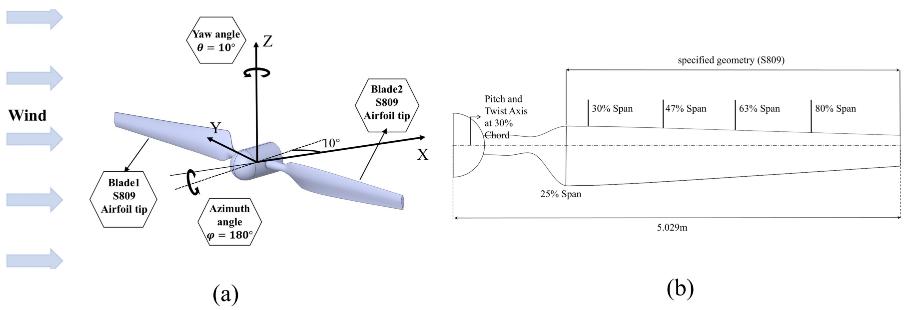

Figure 1. NREL Phase VI wind rotor and blade design. (**a**) Rotor. (**b**) Blade.

Table 1. S809 airfoil unsteady parameter setting.

variable	**value**
Chord[m]	0.457
Reduced Frequencies[Hz]	0.08
Wind Speed[m/s]	33.2
Oscillation Period[s]	1.86
Oscillatory Angle[°]	$\alpha(t) = 12.65 + 10.35\sin(11.62t)$
Reynolds	1×10^6

In this context, k represents the reduced frequency, defined as:

$$k = \frac{\omega c}{2U_0}, \tag{1}$$

where ω is the oscillation frequency, c is the chord length, and U_0 is the free–stream velocity.

In the calculation of the aerodynamics of the entire rotor blade, the AeroDyn module requires the discretization of the blade into multiple smaller airfoil elements, each with consistent aerodynamic properties. By combining the spatial structure and aerodynamic characteristics of each element, variables such as rotor wind speed, rotational speed, yaw angle, and pitch angle are specified, leading to the output of the aerodynamic loads on the blade sections. Figure 2 illustrates the two types of airfoils that form the blade, along with their segmentation into 21 elements. Figure 3 provides a schematic of the local angles and force components at the blade section, where l and d represent lift and drag, respectively, n and t denote the normal and tangential forces, and x and y correspond to the normal and tangential directions of the current plane.

https://doi.org/10.5194/wes-2025-81
Preprint. Discussion started: 27 May 2025

WIND ENERGY SCIENCE DISCUSSIONS

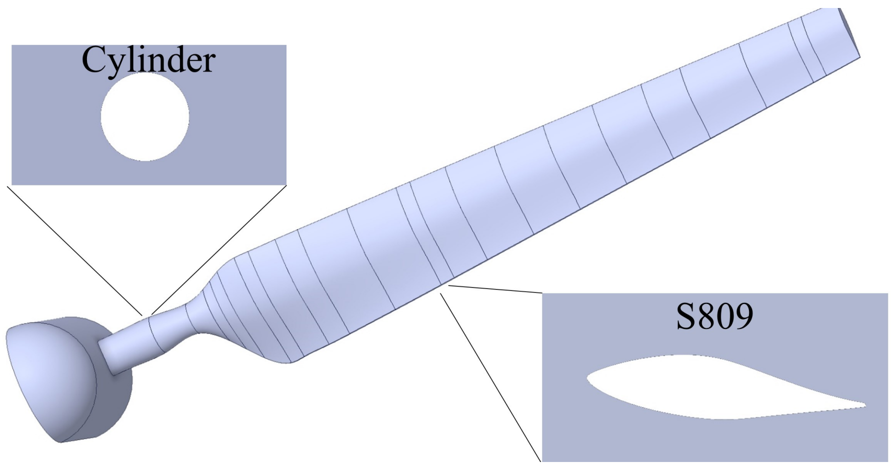

Figure 2. Phase VI blade airfoil configuration.

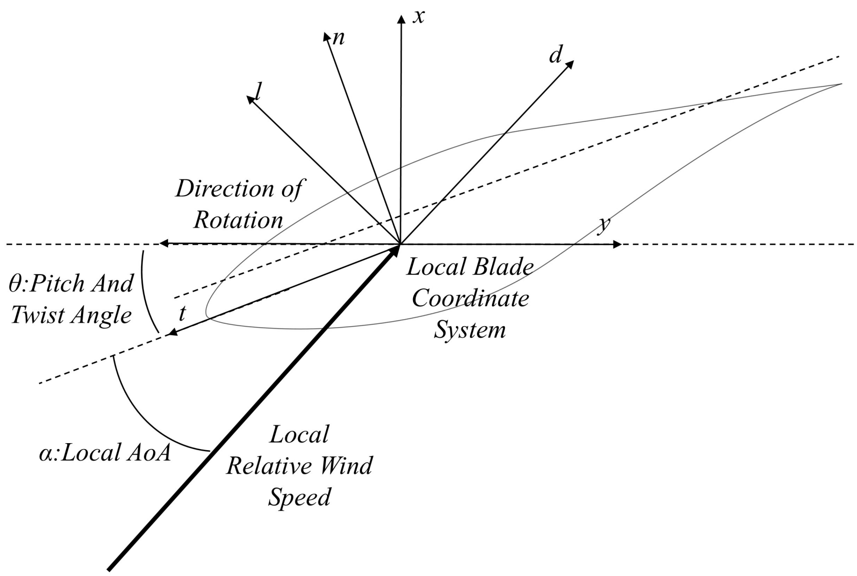

Figure 3. Schematic diagram of blade cross section.

2.2 CFD Method

The CFD simulations were conducted using the ANSYS Fluent software, employing the SST k–ω turbulence model to solve the Navier–Stokes equations. This turbulence model has been widely adopted for wind turbine flow field simulations due to its superior performance in predicting aerodynamic characteristics (Tachos et al., 2010). The Coupled solver method was utilized

https://doi.org/10.5194/wes-2025-81
Preprint. Discussion started: 27 May 2025

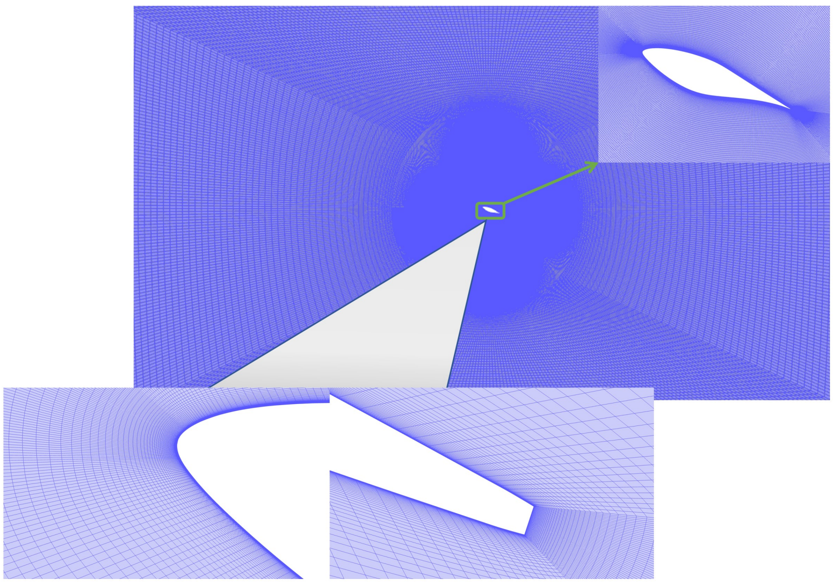

Figure 4. S809 airfoil computational mesh.

to enhance numerical stability and convergence. Mesh generation was performed using ANSYS ICEM, in which a structured mesh topology was adopted to ensure both computational accuracy and solution convergence. For the two–dimensional S809 airfoil, the computational domain was designed with both the inlet and outlet boundaries located at a distance of 40 chord lengths from the airfoil to minimize boundary effects. To replicate the wind tunnel experimental conditions, the upper and lower boundaries were treated as solid walls. A structured mesh based on an O–type topology was generated for both the near–wall and far–field regions, as illustrated in Figure 4, with the mesh center located at the quarter–chord point. The chord length of the airfoil was set to $c = 0.457\ \mathrm{m}$. The height of the first grid layer adjacent to the wall was specified as $0.01\ \mathrm{mm}$ to ensure that the dimensionless wall distance y^+ is approximately 1. To simulate the pitching motion of the airfoil, a User–Defined Function (UDF) was employed in Fluent to impose a time–dependent sinusoidal oscillation within the rotational domain. The pitching motion is defined by the following equation:

$$\alpha(t) = \alpha_0 + A\sin(\omega t), \tag{2}$$

where $\alpha(t)$ is the instantaneous angle of attack, α_0 is the mean angle of attack, A is the oscillation amplitude, and ω is the angular frequency of oscillation.

For the wind turbine rotor, the computational domain was constructed as a cylindrical volume with a diameter of $5D$ and a length of $10D$, as shown in Figure 5, where D represents the diameter of the rotor sweep area. The distance from the rotor plane to the inlet boundary was set to $3D$ to minimize the influence of the inflow boundary. An overset mesh technique was employed to handle the interface between the rotating and stationary domains. Within the rotating region, the mesh around the

https://doi.org/10.5194/wes-2025-81
Preprint. Discussion started: 27 May 2025

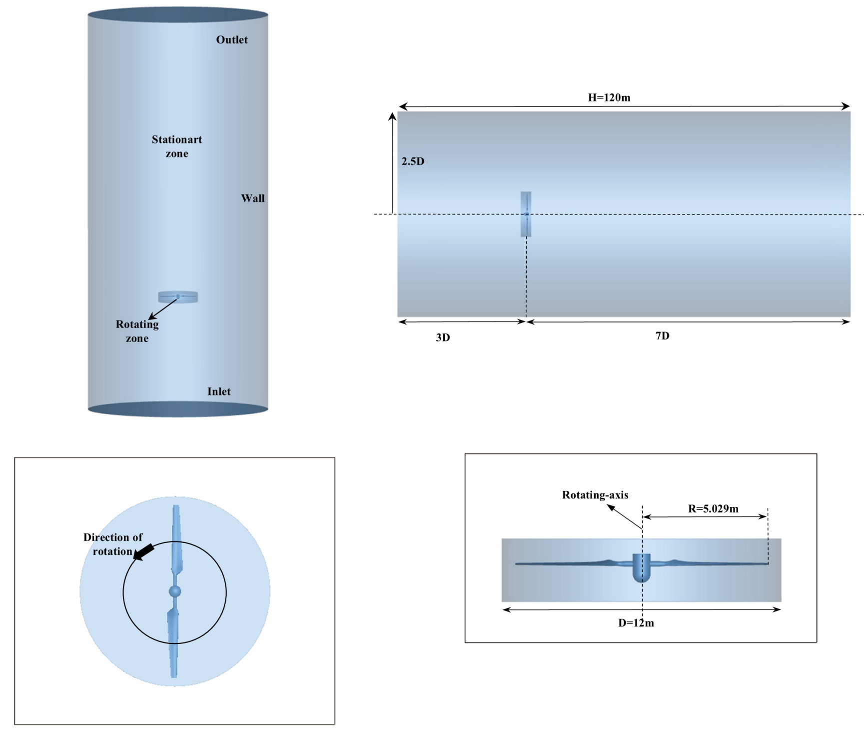

Figure 5. Computational domain in the CFD simulations.

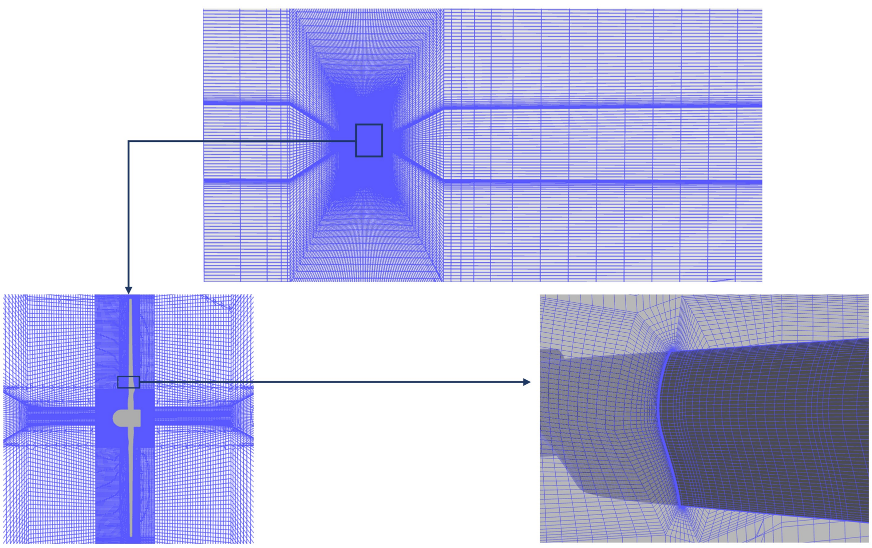

Figure 6. Illustration of wind turbine computational grids.

https://doi.org/10.5194/wes-2025-81
Preprint. Discussion started: 27 May 2025

eawe european academy of wind energy
Open Access WIND ENERGY SCIENCE DISCUSSIONS

blades was generated using an O–type topology, as illustrated in Figure 6. The sectional normal force coefficient C_n on the blade elements was approximated using the following equation:

$$C_n = \frac{F_n}{\frac{1}{2}\rho V^2 S}, \tag{3}$$

where $F_n$is the normal force acting on the blade section, ρ is the air density, V is the relative velocity at the section, and $S$is the projected area of the blade element.

3 Results and Analysis

In this section, the aerodynamic characteristics of the two–dimensional S809 airfoil and the three–dimensional Phase VI wind turbine blades are analyzed based on the BEM and CFD simulations configured in the previous section. The computational results are compared with the wind tunnel experimental data from the NREL Phase VI project. Furthermore, detailed flow field information obtained from the CFD simulations is examined to investigate the evolution of unsteady aerodynamic phenomena and to evaluate their impact on the prediction accuracy of aerodynamic loads.

3.1 Dynamic Stall Validation of the Two–Dimensional Airfoil

In the two–dimensional airfoil simulations, the B–L model and CFD were configured under identical motion conditions. The computational results are compared with experimental data, as shown in Figure 7, which presents the variations of the lift coefficient (C_l) and drag coefficient (C_d) with the angle of attack (AoA, denoted by α) obtained by different methods. From the figure, it can be observed that C_l begins to deviate around $\alpha = 16°$ and drops sharply at approximately $18°$, while $C_d$exhibits a marked increase starting at $\alpha = 16°$, indicating that stall occurs near this AoA Prior to stall, the predictions from both the UAM model, which incorporates a variant of the B–L semi–empirical formulation, and the Fluent CFD simulations show good agreement with the experimental data, although the predicted lift coefficients are slightly lower than the experimental measurements. As the AoA continues to increase, discrepancies emerge between the predicted aerodynamic forces and the experimental results. This deviation is primarily attributed to two factors: (1) the B–L model and the RANS–based CFD simulations have limitations in accurately capturing the vortex evolution during dynamic stall; (2) the experimental data were extracted from three–dimensional wing sections, introducing discrepancies due to three–dimensional nonlinear flow effects not accounted for in two–dimensional simulations. Despite these differences, the overall trends predicted by both methods exhibit good consistency with the experimental observations. Compared to the B–L semi–empirical model, the CFD simulations capture the onset of stall with higher accuracy. In particular, within the range $18° \leq \alpha \leq 23°$, the CFD results more accurately reflect the post–stall fluctuations in lift and drag coefficients. This highlights a better capability in resolving the influence of vortex dynamics on the aerodynamic characteristics after stall. To further investigate the flow mechanisms underlying the dynamic stall process, four representative points with distinct aerodynamic behaviors were selected from the C_l–α curve shown in Figure 7(b). The flow field characteristics at these angles of attack–$18.89°$, $22.73°$, $22.70°$, and $18.74°$–are illustrated in Figure 8 through pressure contours and streamline visualizations.

https://doi.org/10.5194/wes-2025-81
Preprint. Discussion started: 27 May 2025

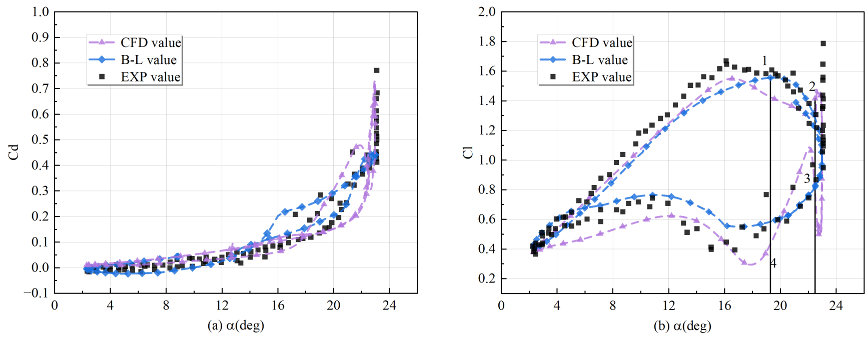

Figure 7. Comparison of CFD and BEM calculation results:(**a**)Drag coefficient.(**b**)Lift coefficient.

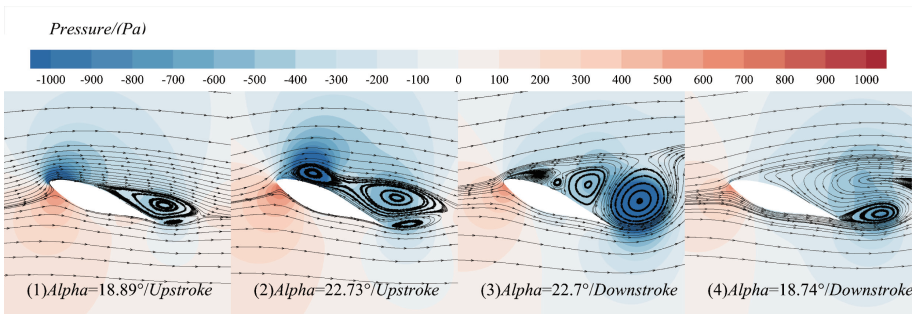

Figure 8. Dynamic stall pressure and vortex evolution diagram.

At point 1 (18.89°), as the AoA increases, low–pressure regions begin to develop near both the leading and trailing edges. A clockwise vortex forms at the trailing edge, initiating a slight decrease in C_l. As the angle further increases to point 2 (22.73°), a leading–edge vortex (LEV) emerges and rapidly expands, merging with the trailing–edge vortex. This interaction generates a large low–pressure zone over the upper surface, resulting in a rapid increase in C_l.

Between points 3 and 4 (from 22.70° to 18.74°), complex vortex shedding occurs, leading to pronounced oscillations in the aerodynamic forces. Notably, the CFD simulations capture these unsteady vortex dynamics with high fidelity, whereas the semi–empirical B–L model fails to resolve the detailed flow separation and reattachment processes. After point 4, as the AoA decreases, the flow gradually reattaches to the airfoil surface, and C_l recovers accordingly.

These results highlight the critical role of vortex formation, evolution, and shedding in governing the dynamic stall behavior, which cannot be fully captured by simplified models such as B–L, emphasizing the necessity of high–fidelity CFD simulations for accurate dynamic stall prediction.

https://doi.org/10.5194/wes-2025-81
Preprint. Discussion started: 27 May 2025

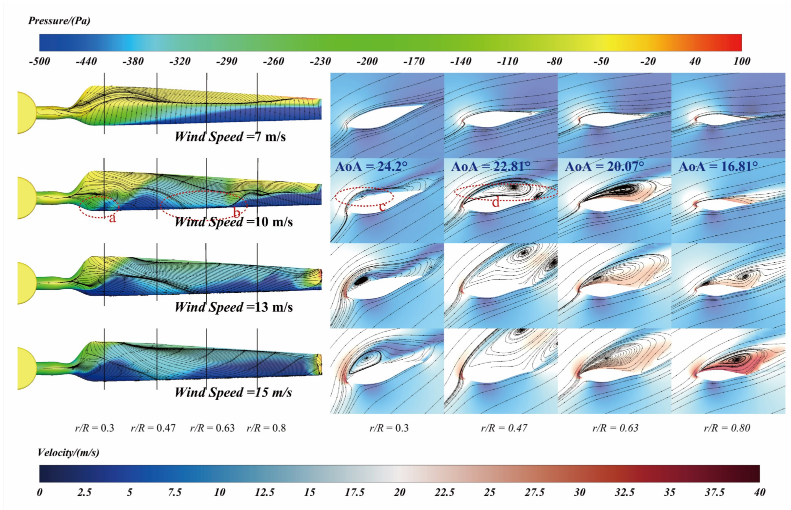

Figure 9. Surface pressure and vorticity distribution on the blade, with streamlines illustrated at four representative spanwise sections.

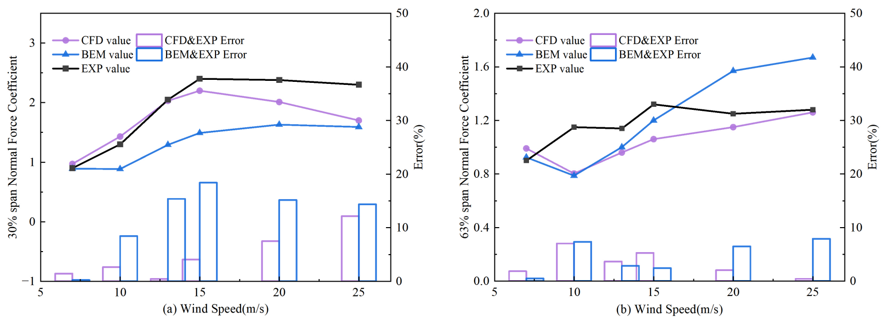

Figure 10. Comparison of normal force coefficient predictions by CFD and BEM under steady conditions at different inflow velocities, for two blade sections: (a) 30% span ($0.3R$) and (b) 63% span ($0.63R$). The corresponding prediction errors relative to experimental data are also shown.

3.2 Three–Dimensional Aerodynamic Characteristics under Non–Yawed Conditions

Figure 9 presents the CFD results for the Phase VI wind turbine rotor under non–yawed conditions, displaying surface–limited streamlines and surface pressure distributions on the blades at various inflow velocities. Four cross–sections located at $0.30\,R$, $0.47\,R$, $0.63\,R$, and $0.80\,R$ along the blade span were selected for detailed analysis. The right–hand panels in Figure 9 show the chordwise velocity contours and streamlines at each section.

The results reveal that, for a constant inflow velocity, the stall intensity along the blade span first increases and then decreases, exhibiting a pattern of weaker stall near the root and tip and stronger stall near the mid–span. Analysis of the streamline patterns indicates that blade rotation induces a spanwise pressure gradient and centrifugal forces, promoting spanwise flow. Near the

https://doi.org/10.5194/wes-2025-81
Preprint. Discussion started: 27 May 2025

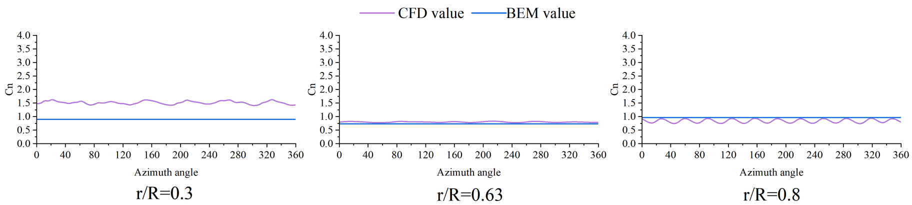

Figure 11. Comparison of unsteady normal force coefficient predictions by CFD and BEM at different blade sections under an inflow velocity of $10\ \mathrm{m/s}$.

blade root, the centrifugal effect is more pronounced, and the chordwise velocity is lower, stabilizing the spanwise vortices along the blade and delaying flow separation. Consequently, the onset of stall is suppressed. In contrast, near the blade tip, although the chordwise velocity is higher and spanwise effects are weaker, the local airfoil sections operate at lower angles of attack, which also mitigates stall development. At an inflow velocity of $7\ \mathrm{m/s}$, flow separation initiates near the mid–chord region, but the flow over the entire blade remains mostly attached, with no significant stall observed. As the inflow velocity increases to $10\ \mathrm{m/s}$, noticeable changes appear in the pressure distributions. At region (a), a sharp pressure drop occurs at the leading edge. At region (b), pressure increases near the leading edge, coupled with a pressure decrease near the trailing edge. These pressure features, combined with the chordwise velocity contours at sections (c) and (d), confirm the onset of flow separation and localized stall on the blade surface. Figure 10 presents a comparison of the steady–state normal force coefficients (C_n) computed using CFD and BEM against experimental data at two representative blade sections: near the root ($0.30\,R$) and mid–span ($0.63\,R$). To quantitatively assess the impact of aerodynamic effects on prediction accuracy, two normalized absolute error metrics are introduced:

$$E_c = \frac{|\Delta_e - \Delta_c|}{\Delta_{e,\max}} \tag{4}$$

$$E_b = \frac{|\Delta_e - \Delta_b|}{\Delta_{e,\max}} \tag{5}$$

where Δ_e, Δ_b, and Δ_c denote the experimental, BEM–predicted, and CFD–predicted normal force coefficients, respectively. $\Delta_{e,\max}$ is the maximum experimental C_n value under all conditions (set to 3.5 in this study).

The results show that, at the same blade sections, the stall region progressively expands with increasing inflow velocity. When the blade surface remains fully attached, both BEM and CFD predictions exhibit high accuracy. Specifically, at an inflow velocity of $V_{w0} = 7\ \mathrm{m/s}$, the prediction errors are small, with $E_c < 3\%$ and $E_b < 2\%$, indicating that three–dimensional effects have minimal influence on aerodynamic force predictions under attached flow conditions (Fogarty, 1951; McCroskey, 1971; Snel et al., 1994).

However, once flow separation occurs on the blade surface ($V_{w0} > 7\ \mathrm{m/s}$), the prediction errors rise sharply. At an inflow velocity of $V_{w0} = 15\ \mathrm{m/s}$ near the blade root ($0.30\,R$), the BEM prediction error E_b rises to approximately 20%. Across all conditions, CFD simulations consistently yield lower prediction errors E_c than BEM. Figures 11 and 12 show the unsteady aerodynamic results at different blade sections under inflow velocities of $10\ \mathrm{m/s}$ and $15\ \mathrm{m/s}$, respectively. At $10\ \mathrm{m/s}$, the

https://doi.org/10.5194/wes-2025-81
Preprint. Discussion started: 27 May 2025

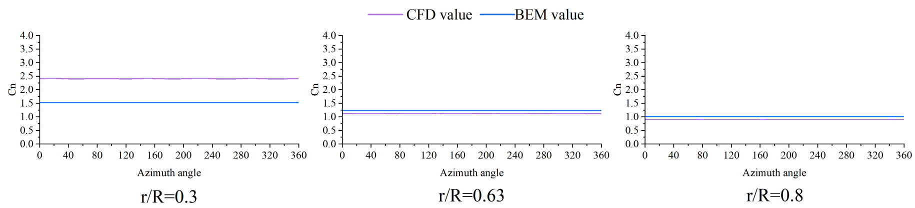

Figure 12. Comparison of unsteady normal force coefficient predictions by CFD and BEM at different blade sections under an inflow velocity of $15\ \mathrm{m/s}$.

CFD–predicted C_n exhibits noticeable fluctuations with azimuthal angle, particularly near the blade root and tip. At the root section, the discrepancy between the CFD and BEM predictions is approximately 0.6–0.8. However, at $15\ \mathrm{m/s}$, the C_n values become nearly independent of the azimuthal position. The discrepancy between CFD and BEM predictions at the root increases to approximately 0.9. The predicted C_n values are slightly higher than those obtained from steady–state simulations.

These results suggest that the coupling effects of three–dimensional rotational phenomena and dynamic stall significantly influence the aerodynamic predictions. Nevertheless, due to the absence of corresponding experimental data under these conditions, a quantitative validation of the computational results could not be performed.

3.3 Three–Dimensional Aerodynamic Characteristics under Yawed Conditions

Following the same computational setup as the non–yawed case, CFD simulations were conducted in Fluent by rotating the external flow field by $10°$, $30°$, and $60°$, corresponding to three different yawed configurations of the wind turbine. Figures 13(a)–(c) illustrate the schematic diagrams for each yaw angle. In the AeroDyn simulations, the yaw angle was set to $10°$, $30°$, and $60°$, while keeping all other input parameters unchanged.

The azimuthal angle $\varphi = 0°$ is defined when blade 1 is positioned at the 3 o'clock direction, as illustrated in Figure 14, based on the blade model in Figure 1.Accordingly, Figure 15 presents the variation of the AoA with azimuthal position φ at different blade sections under the three yawed conditions.

The results reveal that, under yawed conditions, rotor rotation induces a periodic variation in the AoA experienced by each blade element. The amplitude of these fluctuations increases with the yaw angle, while the mean AoA also increases with the inflow velocity. Furthermore, from a spanwise perspective, both the amplitude and the mean value of AoA decrease toward the blade tip. Overall, the inflow characteristics at each blade section are primarily governed by the yaw angle and the inflow velocity.

When the blade azimuthal angle φ is in regions 3 and 4 ($180° < \varphi < 360°$), the blade operates on the leeward side of the rotor. During rotation, the inflow velocity component parallel to the rotor plane (the X–direction as defined in Figure 14) partially cancels out the tangential velocity component of the blade, reducing the relative velocity between the airflow and the blade. When the azimuthal angle reaches $\varphi = 270°$, the blade velocity vector becomes aligned with the inflow velocity along the rotor plane (X–axis), resulting in the minimum relative velocity and, consequently, the maximum AoA for the blade

https://doi.org/10.5194/wes-2025-81
Preprint. Discussion started: 27 May 2025

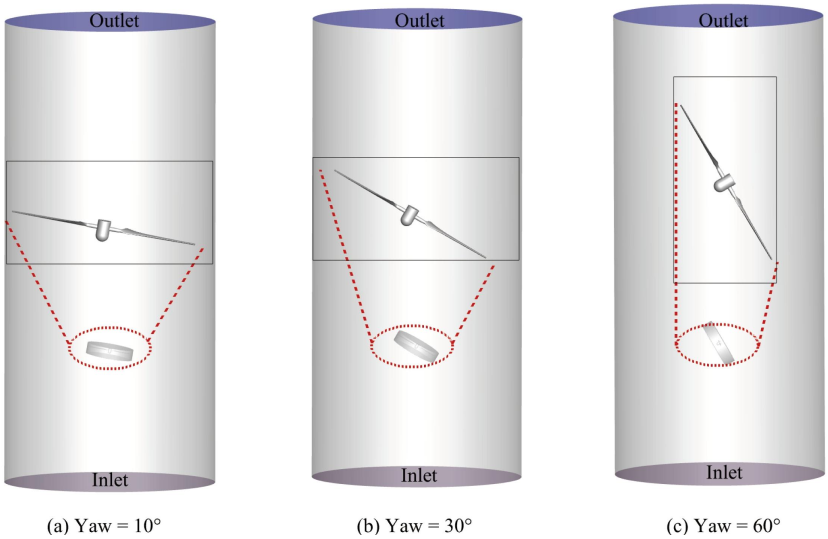

Figure 13. Schematic diagrams of the rotor under three yawed inflow conditions: (a) 10°, (b) 30°, and (c) 60°.

section. Conversely, when the blade is in regions 1 and 2 ($0° < \varphi < 180°$), it operates on the windward side of the rotor. In this case, the blade's tangential velocity and the inflow component act in the same direction, thereby increasing the relative velocity experienced by the blade. At $\varphi = 90°$, the blade velocity vector is directly opposed to the inflow velocity component along the X–axis. As a result, the relative velocity reaches its maximum, and the AoA correspondingly attains its minimum value. Figures 16 and 17 present the variations of the C_n with azimuthal angle φ predicted by CFD and BEM methods under inflow velocities of $V_{w0} = 10\ \mathrm{m/s}$ and $V_{w0} = 15\ \mathrm{m/s}$, respectively, for different yaw angles.

Analysis of the computational results shows that an increase in inflow velocity leads to a rise in both the amplitude and the mean value of C_n. However, excessively high inflow velocities can trigger flow separation and dynamic stall on the blades. This behavior is closely related to the variation of the AoA with inflow velocity discussed earlier.At $V = 10\ \mathrm{m/s}$, none of the four blade sections exhibit significant stall characteristics under any of the three yaw angles, with C_n maintaining smooth periodic variations. In contrast, at $V = 15\ \mathrm{m/s}$, dynamic stall phenomena become apparent, particularly under yaw angles of 30° and 60°. As observed in the corresponding plots, C_n reaches a peak before the azimuthal angle $\varphi = 270°$ (the point of maximum AoA) and subsequently experiences a sudden drop, indicating the occurrence of dynamic stall on the blade sections.

Furthermore, the amplitude of C_n fluctuations and the severity of stall decrease toward the blade tip for different yaw angles. As a result, the prediction accuracy of both BEM and CFD methods improves with increasing radial position.

At the blade root section ($0.3R$), relatively large discrepancies are observed between BEM and CFD predictions. Although both methods exhibit errors, the CFD results more closely match the experimental data in terms of the qualitative trend along the azimuthal angle. At mid–span sections ($0.47R$ and $0.63R$), the prediction accuracy of both methods improves significantly, with the CFD performance being slightly superior at $0.63R$ compared to $0.47R$. Under high yaw and high inflow velocity

https://doi.org/10.5194/wes-2025-81
Preprint. Discussion started: 27 May 2025

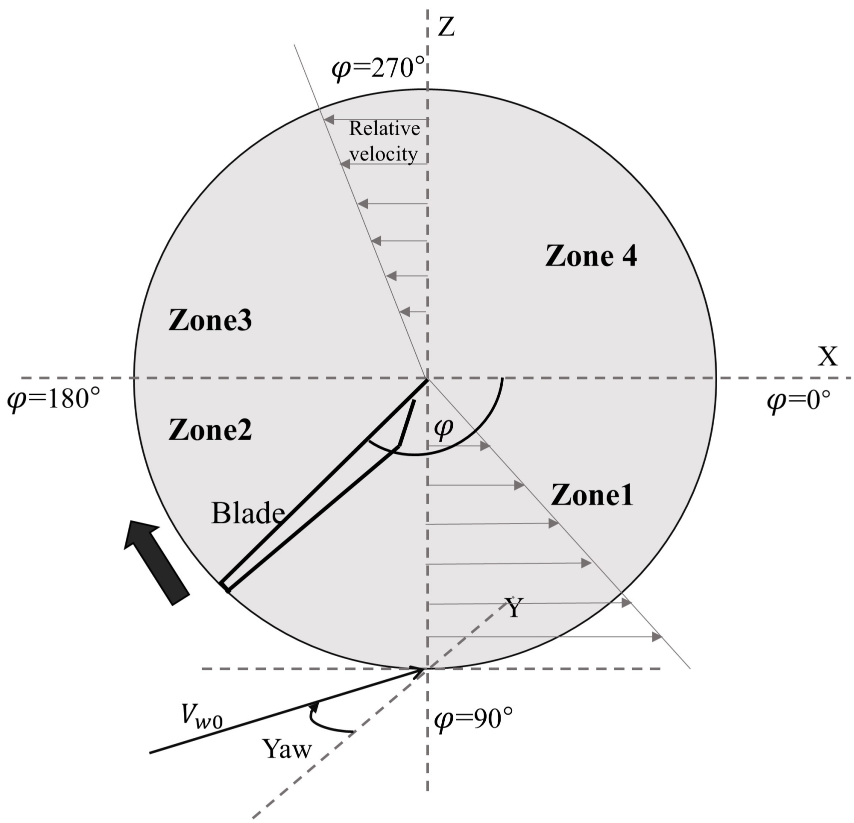

Figure 14. Schematic diagrams of the rotor illustrating blade positions at various azimuthal angles and their corresponding inflow (windward) orientations. The figure provides an overview of blade motion and inflow encounter during a full rotation cycle.

conditions ($15\ \mathrm{m/s}$, $60°$), the maximum BEM prediction error (E_b) at $0.63R$ occurs on the leeward side, reaching values exceeding 18%.

For the blade tip section ($0.8R$, the maximum E_b value also occurs on the leeward side under the same extreme conditions, but is slightly lower, approximately 14.3%.

245 To evaluate the impact of yawed inflow on the predictive capability of the BEM model, which accounts for three–dimensional rotational effects and dynamic stall, the simulation results under yawed conditions were compared against those under non–yawed conditions. Table 2 summarizes the maximum prediction errors (E_b) for each operating condition.

https://doi.org/10.5194/wes-2025-81
Preprint. Discussion started: 27 May 2025

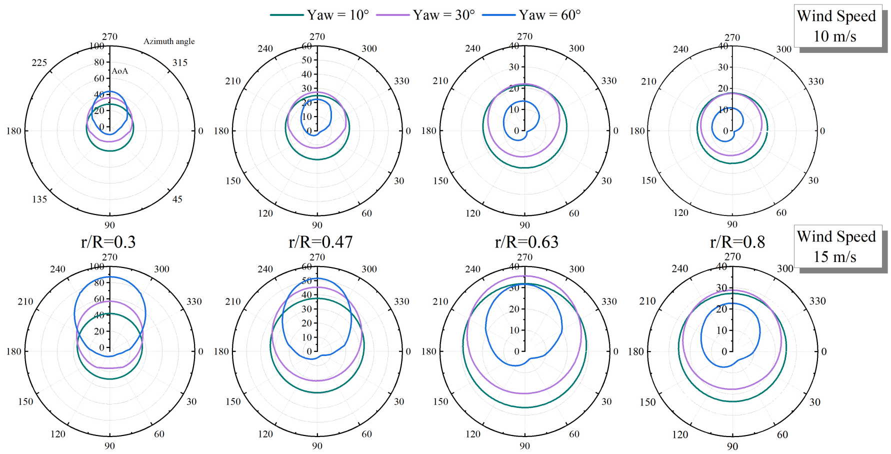

Figure 15. Variation of AoA with azimuthal position at different blade sections under three yaw angles: 10°, 30°, and 60°.

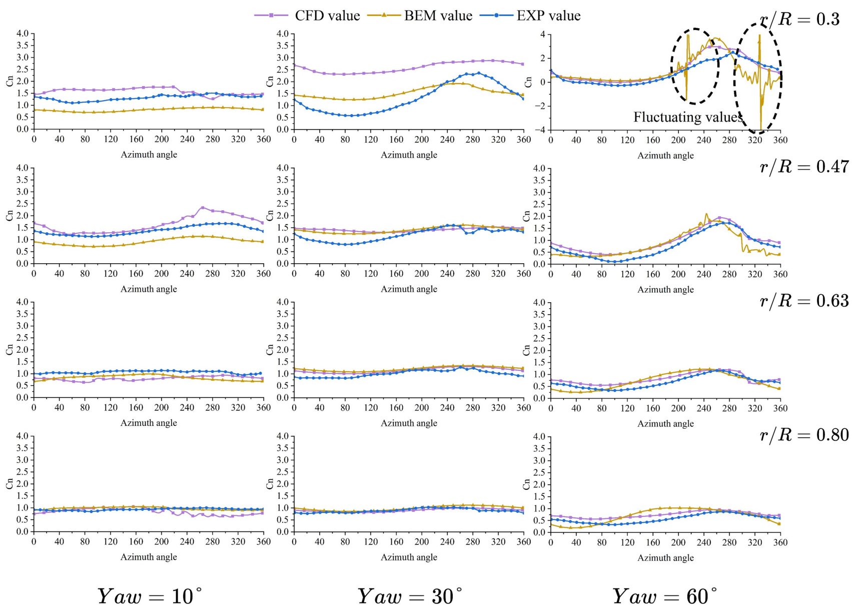

Figure 16. Variation of the normal C_n with azimuthal angle at different yaw angles, as predicted by CFD and BEM methods under an inflow velocity of $10\ \mathrm{m/s}$.

3.4 Unsteady Vortex Evolution and Aerodynamic Prediction Error Analysis

To further investigate the influence of yawed inflow on prediction errors, CFD–simulated flow fields, which exhibit closer agreement with experimental data, were utilized to analyze the effects of yawed inflow on three–dimensional rotational phenomena and dynamic stall.

https://doi.org/10.5194/wes-2025-81
Preprint. Discussion started: 27 May 2025

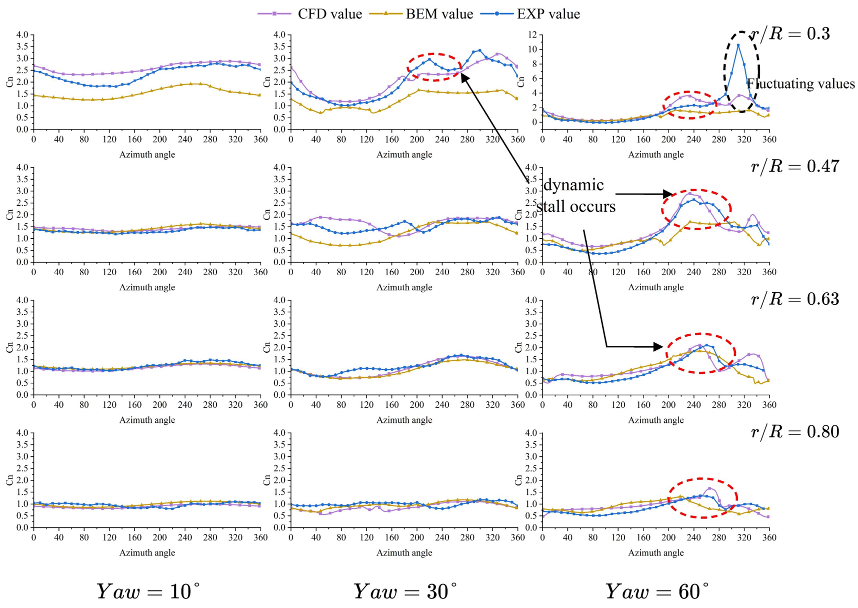

Figure 17. Variation of the normal C_n with azimuthal angle at different yaw angles, as predicted by CFD and BEM methods under an inflow velocity of $15\ \mathrm{m/s}$.

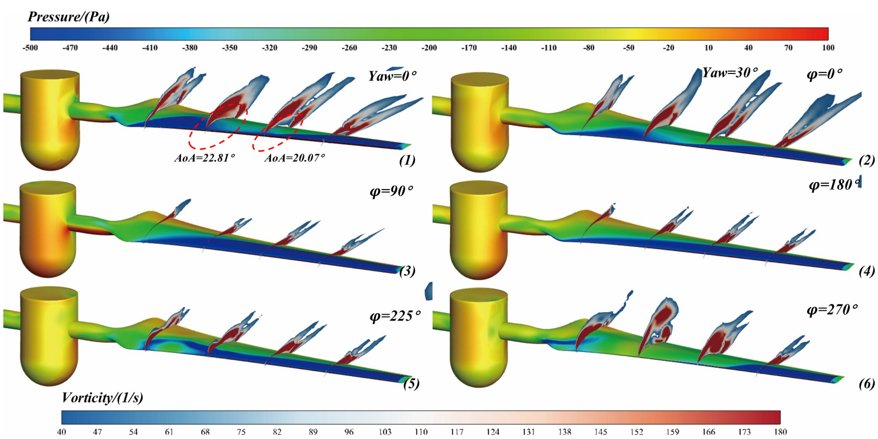

Figure 18. Vorticity contour slices at different blade sections and azimuthal positions under non-yawed and 30° yawed inflow conditions.

Figure 18 compares the vorticity distributions of blade sections under yawed inflow at $V_{w0} = 10\ \mathrm{m/s}$ for a yaw angle of 30°, where subplots (2)–(6) represent the vorticity fields at different azimuthal angles.

According to experimental data, the static stall angle of the NREL S809 airfoil is approximately $15.2°$. From the streamline patterns at the $0.3R$ section in Figure 9, it is observed that, under rotational effects, the stall angle at this section shifts to

https://doi.org/10.5194/wes-2025-81
Preprint. Discussion started: 27 May 2025

Table 2. Comparison of normal force prediction errors between BEM and CFD at different yaw angles, inflow velocities, and blade sections.

	Yaw=0(E_b/E_c)	**Yaw=0**(E_b/E_c)	**Yaw=0**(E_b/E_c)	**Yaw=0**(E_b/E_c)
$10\ \mathrm{m/s}, 0.3R$	8.4%/3.8%	21.4%/14.3%	24.3%/35.7%	48.5%/31.4%
$10\ \mathrm{m/s}, 0.63R$	6.3%/7.3%	10.3%/11.4%	11.6%/8.6%	11.2%/9.4%
$15\ \mathrm{m/s}, 0.3R$	18.3%/0.4%	34.3%/14.3%	48.6%/18.6%	192.9%/271.4%
$15\ \mathrm{m/s}, 0.63R$	4.6%/2.4%	5.6%/7.1%	11.2%/10.8%	18.6%/15.7%

approximately $24°$. This clearly demonstrates that three–dimensional rotational effects coupled with unsteady aerodynamic phenomena induce stall delay.

Furthermore, based on the results in Figure 15, at a yaw angle of 30°and an azimuthal angle of $\varphi = 225°$, the angles of attack at $0.3R$, $0.47R$, $0.63R$, and $0.8R$ are approximately 32°, 26°, 22°, and 17°, respectively. These AoA values are significantly higher than those under non–yawed conditions. However, as shown in Figure 18, the stall intensity observed at $\varphi = 225°$ is notably weaker compared to the non–yawed case.

This indicates that in the presence of yawed inflow, the coupling between the incoming flow and blade rotation introduces significant three–dimensional unsteady effects, which substantially alter the stall characteristics and delay the onset of severe flow separation.

To further elucidate the influence of yaw–induced three–dimensional unsteady structures on the aerodynamic loads of wind turbine blades, cases with significant stall effects ($V_{w0} > 15\ \mathrm{m/s}$) were selected for detailed analysis. Under these conditions, the prediction errors between CFD and BEM are more pronounced, providing higher significance for comparative studies.

During each rotational cycle, eight azimuthal angles were analyzed, with an interval of $45°$ between successive positions, to capture the evolution of the flow features. Figure 19 presents the iso–surfaces of the Q–criterion under different yaw angles, where the color contours represent the magnitude of velocity.

Figure 19a shows the flow structures under non–yawed conditions. It can be observed that, with varying azimuthal angles, neither the vortex wake shape nor the velocity distribution exhibits significant changes. In the absence of yaw–induced disturbances, the aerodynamic loads on the blades remain relatively insensitive to azimuthal variations, which is consistent with the unsteady simulation results presented in Figur 12.

Figure 19b illustrates the case with a yaw angle of $10°$. The separated vortices observed under this condition are similar to those in the non–yawed case, and the unsteady aerodynamic effects remain minor. According to the computational results in Figure 17, the amplitude of C_n variations remains stable under $10°$ yaw, and the prediction errors between CFD and BEM at the blade root section range between 0.8 and 1.2, comparable to the non–yawed case.

When the yaw angle increases to $30°$, the numerical results indicate that the BEM predictions at the blade root on the windward side become more accurate compared to the non–yawed condition. At an azimuthal angle of $\varphi = 90°$, the difference

https://doi.org/10.5194/wes-2025-81
Preprint. Discussion started: 27 May 2025

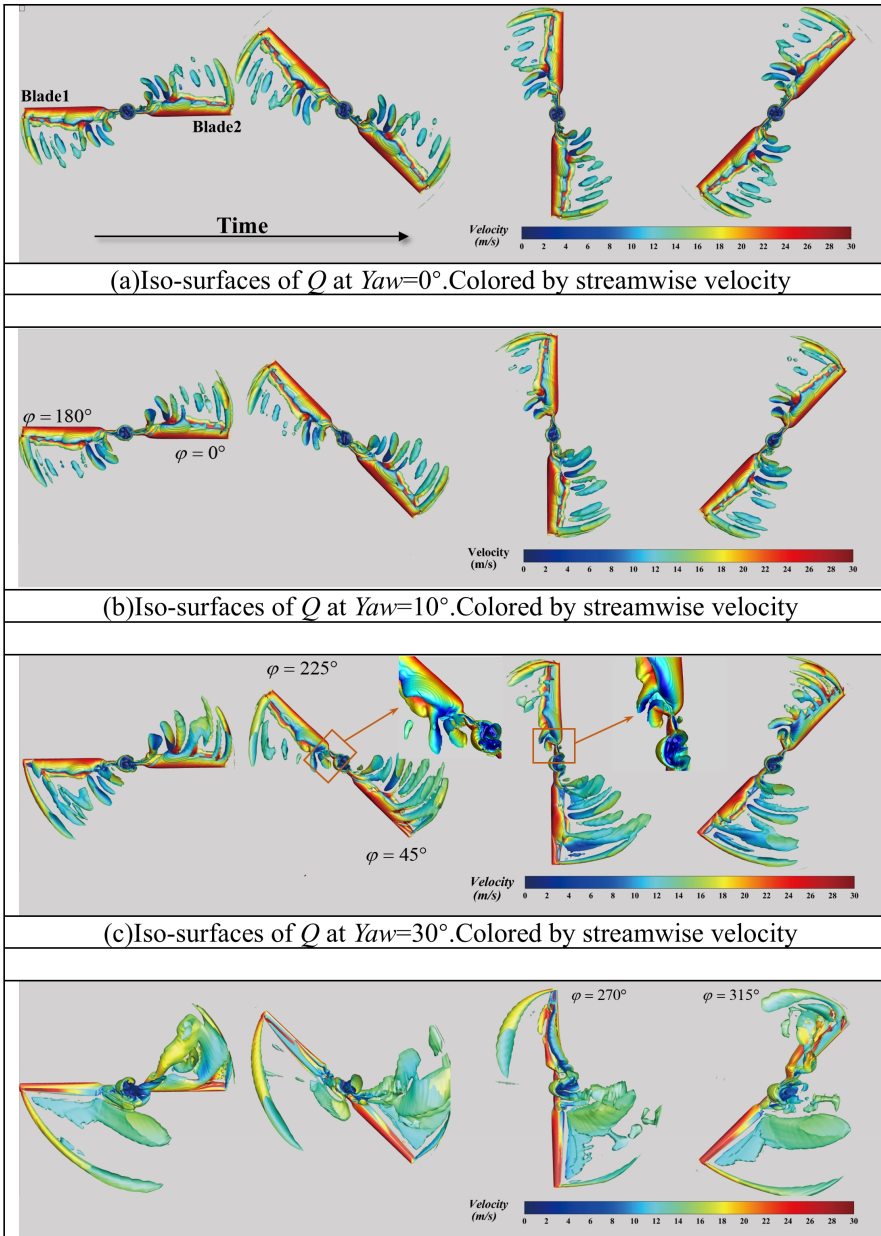

(a)Iso-surfaces of Q at *Yaw*=0°.Colored by streamwise velocity

(b)Iso-surfaces of Q at *Yaw*=10°.Colored by streamwise velocity

(c)Iso-surfaces of Q at *Yaw*=30°.Colored by streamwise velocity

(d)Iso-surfaces of Q at *Yaw*=60°.Colored by streamwise velocity

Figure 19. Iso-surfaces of the Q-criterion under different yaw angles: (a) 0°, (b) 10°, (c) 30°, and (d) 60°, illustrating the evolution of vortex structures across increasing yaw misalignment.

in C_n between the BEM and CFD predictions is only about 0.3. However, on the leeward side, the maximum discrepancy between BEM and CFD predictions can reach up to 1.5.

https://doi.org/10.5194/wes-2025-81
Preprint. Discussion started: 27 May 2025

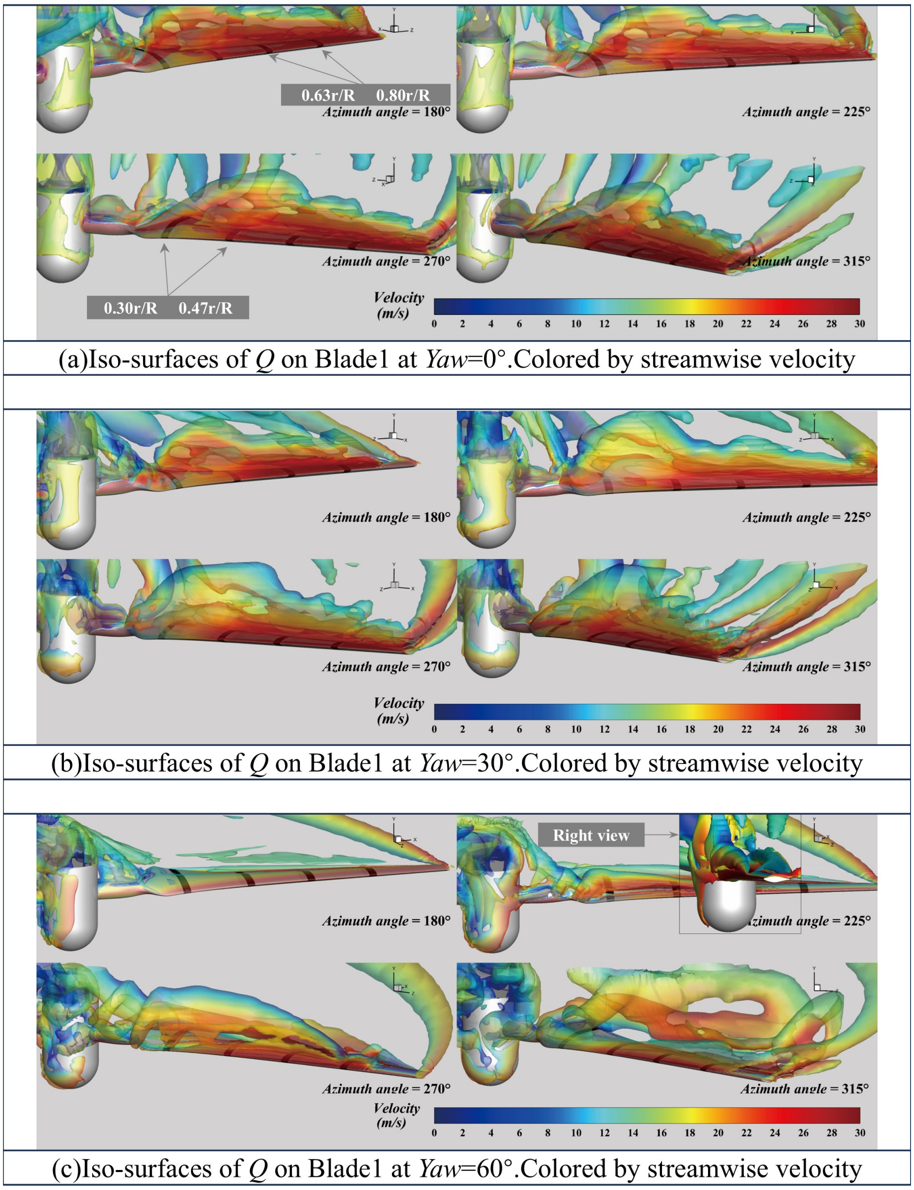

Figure 20. Iso-surfaces of the Q-criterion over the blade in the leeward region (180°–360° azimuthal angle) under different yaw angles: (a) 0°, (b) 30°, and (c) 60°. The results highlight the influence of yaw on vortex evolution and spanwise interactions on the suction side.

From the analysis of Figure 19c, the vortex wake structures on the windward and leeward sides already show clear differences compared to the non–yawed case due to the coupling between the inflow and blade rotation. These differences become even more pronounced under higher yaw angles, as illustrated in Figure 19d. Correspondingly, at this yaw angle, the prediction error

https://doi.org/10.5194/wes-2025-81
Preprint. Discussion started: 27 May 2025

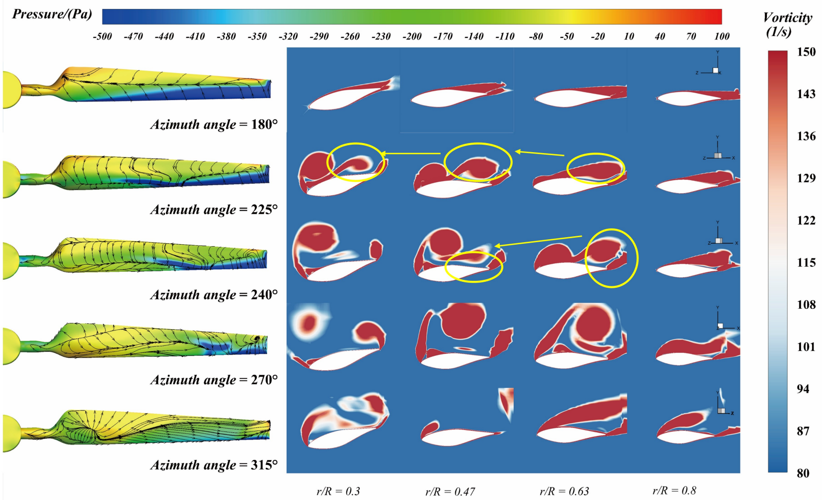

Figure 21. Surface pressure distribution and streamlines over the blade, along with vorticity slices at representative blade sections, under a high yaw angle of 60° and different azimuthal positions. The results reveal the evolution of surface flow features and internal vortex structures during blade rotation in strongly yawed inflow.

in C_n between CFD and BEM exceeds 2 at the blade root ($0.3R$) and also increases significantly at $0.47R$. Similar to previous observations, the prediction errors decrease on the windward side and increase on the leeward side.

Figures 20 and 21 further illustrate the vortex wake structures at blade sections located on the leeward side under high yaw angles, providing deeper insight into the mechanisms leading to increased prediction errors. Based on the vortex patterns at yaw angles of 30° and 60°, it is observed that on the windward side, the flow remains attached to the suction surface of the blade. As the yaw angle increases, the degree of attachment becomes stronger. This phenomenon can be attributed to two factors: (1) the variation of the effective AoA induced by azimuthal rotation under yawed conditions, and (2) the lateral inflow combined with blade rotation, which generates a Coriolis force that mitigates the severity of dynamic stall. Despite the increased flow complexity caused by multiple interacting effects, the BEM model maintains relatively high prediction accuracy for attached flow conditions.

In contrast, on the leeward side, in addition to the tangential inflow due to blade rotation, a lateral inflow component directed from the blade tip toward the blade root is present. The Q–criterion iso–surfaces and sectional vorticity distributions reveal that significant separated vortex structures form on the suction surface at high angles of attack. Unlike the non–yawed case, high yaw angles induce a pronounced spanwise flow component on the suction surface, which, under the influence of the Coriolis force, leads to the formation of a strong spanwise vortex band extending from the blade tip toward the root. As the azimuthal angle progresses, this vortex band rapidly expands across the leeward region of the rotor disk, causing the stalled region to propagate from the tip toward the root, thereby resulting in severe local aerodynamic load fluctuations.

Figure 21 presents the surface streamlines and vorticity contours at different blade sections under these conditions. Compared to the streamlines in Figure 9, it is evident that under the combined effects of yaw and rotation, the interaction between leading–

https://doi.org/10.5194/wes-2025-81
Preprint. Discussion started: 27 May 2025

edge and trailing–edge vortices is significantly enhanced. Additionally, extra intermediate vortices emerge in the leeward region at certain sections, particularly between azimuthal angles of $225°$ and $315°$. These newly formed vortices merge with the original separated vortices and undergo continuous spanwise stretching and shedding, substantially altering the surface pressure distribution and aerodynamic characteristics of the blade. Consequently, this leads to asymmetric periodic fluctuations in the normal force coefficient C_n.

By comparing the evolution of sectional flow fields with the time histories of aerodynamic forces, it is observed that the generation, expansion, and shedding of stall vortices directly correspond to the rapid rise and fall phases of the normal force coefficient C_n. In contrast, the BEM method, which relies on steady–state local airfoil characteristics, fails to capture these strong unsteady dynamics, leading to significant prediction errors in the leeward region.

Under high yaw and high inflow velocity conditions (e.g., $V_{w0} = 15\ \mathrm{m/s}$, $\theta = 30°$), the BEM–predicted error E_b at the blade root exceeds 48%, whereas the CFD simulation results maintain good agreement with the experimental data.

Overall, the analysis reveals that yaw–induced unsteady phenomena not only alter the local AoA and stall behavior but also result in strong unsteady fluctuations in aerodynamic force coefficients due to complex vortex interactions. The conventional corrected BEM method, which neglects three–dimensional unsteady vortex structures, is therefore unable to accurately predict the aerodynamic load variations on wind turbine blades under high yaw conditions.

3.5 Summary

In this chapter, the aerodynamic characteristics and prediction error sources of the Phase VI wind turbine blades under non–yawed and various yawed conditions were systematically analyzed based on CFD simulations and the corrected BEM method.

The results show that when the blades operate under attached flow conditions, the BEM and CFD methods exhibit high consistency in aerodynamic force predictions. For instance, at low inflow velocities and mid–span blade sections, the predicted C_n closely match the experimental data. However, once flow separation and stall occur, the three–dimensional rotational effects and unsteady dynamic stall phenomena become significant, leading to a notable increase in BEM prediction errors.

Under yawed conditions, the periodic variation of the AoA and the complex vortex dynamics further amplify the prediction deviations. At high yaw angles, strong separated vortex structures develop along the blade span from tip to root on the leeward side, breaking the local steady–state assumptions inherent in traditional BEM models and resulting in a substantial increase in aerodynamic force prediction errors near the blade root.

The detailed CFD flow field analyses reveal the direct influence of unsteady stall vortex evolution on aerodynamic force fluctuations, providing important theoretical support for the future improvement of BEM models and enhancing their applicability under complex flow conditions.

4 Conclusions

This study systematically investigated the influence of complex three–dimensional unsteady aerodynamic effects, induced by yawed and non–yawed inflow conditions, on the prediction accuracy of aerodynamic loads on the NREL Phase VI wind turbine

https://doi.org/10.5194/wes-2025-81
Preprint. Discussion started: 27 May 2025

blades. The analysis was conducted using computational fluid dynamics (CFD) simulations and a corrected semi–empirical blade element momentum (BEM) method. Based on two–dimensional airfoil dynamic stall validation, three–dimensional rotor flow field evolution analysis, and aerodynamic force error comparisons, the following conclusions were drawn:

1. Under attached flow conditions, both the corrected BEM method and CFD simulations accurately predict the blade aerodynamic loads, with prediction errors generally below 3%. This confirms the applicability of the local steady–state airfoil assumption in such regimes.

2. When flow separation and stall occur on the blade surface, three–dimensional rotational effects delay stall onset, and spanwise flows suppress vortex shedding. However, the BEM method fails to capture unsteady flow features accurately, leading to a significant increase in prediction errors, especially near the blade root, where errors can reach up to 20

3. Under yawed conditions, the interaction between leading–edge and trailing–edge vortices intensifies, and additional intermediate vortices form in the leeward sections of the blades. Yawed inflow induces a prominent spanwise flow component on the suction surface, which, combined with Coriolis forces, generates a strong vortex band extending from blade tip to root. As the azimuthal angle progresses, this vortex band expands across the leeward side of the rotor disk, causing the stalled region to propagate from tip to root and resulting in severe local aerodynamic load fluctuations. Under high yaw angle (60°) and high inflow velocity ($15\ \mathrm{m/s}$) conditions, the BEM–predicted normal force coefficient error (E_b) at the blade root on the leeward side reaches up to 48.5%, whereas CFD simulations maintain errors within the range of 15% to 30%.

4. Through detailed CFD flow field analyses, this study systematically revealed the spanwise evolution of stall vortices under high yaw conditions and their direct impact on aerodynamic load variations. The findings provide new insights into the aerodynamic response of wind turbines in complex flow environments and clearly highlight the limitations of traditional BEM models in handling yaw–induced unsteady aerodynamic effects.

In conclusion, although the corrected BEM method exhibits good applicability under conventional inflow conditions, it shows significant limitations under complex three–dimensional yawed flow environments. Future work can build on the vortex dynamics revealed in this study to develop new BEM models incorporating unsteady rotational effects and spanwise vortex corrections. In addition, combining artificial intelligence techniques for flow field modeling and rapid corrections may further enhance the prediction accuracy and reliability of wind turbine aerodynamic performance in engineering applications. Moreover, large eddy simulation (LES) techniques could be employed to further investigate detailed high–yaw vortex dynamics, providing a stronger physical basis for the development of next–generation high–fidelity BEM methods.

Author contributions. JH:setup and conduction of simulations, formal analysis,and writing.HY:supervision and technical review. JY supervision and technical review.

https://doi.org/10.5194/wes-2025-81
Preprint. Discussion started: 27 May 2025

Competing interests. The authors declare that they have no conflict of interest.

Disclaimer. Publisher's note: Copernicus Publications remains neutral with regard to jurisdictional claims made in the text, published maps, institutional affiliations, or any other geographical representation in this paper. While Copernicus Publications makes every effort to include appropriate place names, the final responsibility lies with the authors.

Acknowledgements. The authors declare that no financial support was received for the research, authorship, and/or publication of this article.

https://doi.org/10.5194/wes-2025-81
Preprint. Discussion started: 27 May 2025

References

Amoretti, T., Huet, F., Garambois, P., and Roucoules, L.: Configurable dual rotor wind turbine model based on BEM method: Co-rotating and counter-rotating comparison, Energy Conversion and Management, 293, 117 461, https://doi.org/10.1016/j.enconman.2023.117461, 2023.

Bangga, G., Lutz, T., and Arnold, M.: An improved second-order dynamic stall model for wind turbine airfoils, Wind Energy Science, 5, 1037–1058, https://doi.org/10.5194/wes-5-1037-2020, 2020.

Chehouri, A., Younes, R., Ilinca, A., and Perron, J.: Review of performance optimization techniques applied to wind turbines, Applied Energy, 142, 361–388, https://doi.org/10.1016/j.apenergy.2014.12.043, 2015.

Dai, Y., Zhong, L., Li, B., Deng, Z., Wang, J., and Zhao, C.: An analysis of the effects of a fused blade tip construction on a wind turbine's aerodynamic performance and wake flow characteristics was carried out, Ocean Engineering, 313, 119 464, https://doi.org/10.1016/j.oceaneng.2024.119464, 2024.

Damiani, R., Hayman, G., Wang, Q., and Jonkman, J. M.: Development and validation of a new unsteady airfoil aerodynamics model within aerodyn, in: 34th Wind Energy Symposium, p. 1007, https://doi.org/10.2514/6.2016-1007, 2016.

Du, Z. and Selig, M.: A 3-D stall-delay model for horizontal axis wind turbine performance prediction, in: 1998 ASME Wind Energy Symposium, p. 21, https://doi.org/10.2514/6.1998-21, 1998.

Elgammi, M., Sant, T., and Alshaikh, M.: Predicting the stochastic aerodynamic loads on blades of two yawed downwind hawts in uncontrolled conditions using a bem algorithm, Renewable Energy, 146, 371–383, https://doi.org/10.1016/j.renene.2019.06.114, 2020.

Fogarty, L. E.: The laminar boundary layer on a rotating blade, Journal of the Aeronautical Sciences, 18, 247–252, https://doi.org/10.2514/8.1921, 1951.

GIanert, H.: Airplane propellers, 1935.

Ji, B., Zhong, K., Xiong, Q., Qiu, P., Zhang, X., and Wang, L.: CFD simulations of aerodynamic characteristics for the three-blade NREL Phase VI wind turbine model, Energy, 249, 123 670, https://doi.org/10.1016/j.energy.2022.123670, 2022.

Laalej, S., Bouatem, A., AlMers, A., and El Maani, R.: Wind turbine performances prediction using BEM approach with Jonkman-Buhl brake state model coupled to CFD method, Materials Today: Proceedings, 65, 3829–3838, https://doi.org/10.1016/j.matpr.2022.07.033, 2022.

Leishman, J. and Beddoes, T.: A generalised model for airfoil unsteady aerodynamic behaviour and dynamic stall using the indicial method, in: Proceedings of the 42nd Annual forum of the American Helicopter Society, vol. 34, pp. 3–17, Washington DC, 1986.

Liu, X., Liang, S., Li, G., Godbole, A., and Lu, C.: An improved dynamic stall model and its effect on wind turbine fatigue load prediction, Renewable energy, 156, 117–130, https://doi.org/10.1016/j.renene.2020.04.040, 2020.

Malik, T. H. and Bak, C.: Challenges in detecting wind turbine power loss: the effects of blade erosion, turbulence, and time averaging, Wind Energy Science, 10, 227–243, https://doi.org/10.5194/wes-10-227-2025, 2025.

Mancini, S., Boorsma, K., Schepers, G., and Savenije, F.: A comparison of dynamic inflow models for the blade element momentum method, Wind Energy Science, 8, 193–210, https://doi.org/10.5194/wes-8-193-2023, 2023.

McCroskey, W. J.: Measurements of boundary layer transition, separation and streamline direction on rotating blades, vol. 6321, National Aeronautics and Space Administration, 1971.

Monteiro, J., Páscoa, J., Brójo, F. R., et al.: Simulation of the aerodynamic behaviour of a micro wind turbine, RE&PQJ, 7, 2009.

Özkan, R. and Genç, M. S.: Aerodynamic design and optimization of a small-scale wind turbine blade using a novel artificial bee colony algorithm based on blade element momentum (ABC-BEM) theory, Energy Conversion and Management, 283, 116 937, https://doi.org/10.1016/j.enconman.2023.116937, 2023.

Potentier, T., Guilmineau, E., Finez, A., Le Bourdat, C., and Braud, C.: High-Reynolds-number wind turbine blade equipped with root spoilers – Part 2: Impact on energy production and turbine lifetime, Wind Energy Science, 7, 1771–1790, https://doi.org/10.5194/wes-7-1771-2022, 2022.

Ram, K. R., Lal, S. P., and Ahmed, M. R.: Design and optimization of airfoils and a 20 kW wind turbine using multi-objective genetic algorithm and HARP_Opt code, Renewable Energy, 144, 56–67, https://doi.org/10.1016/j.renene.2018.08.040, 2019.

Selvatici, D. and Stevens, R. J.: Capturing tip-corrected blade element momentum loading with wind turbine models, Renewable Energy, 241, 122 265, https://doi.org/10.1016/j.renene.2024.122265, 2025.

Simms, D., Schreck, S., Hand, M., and Fingersh, L. J.: NREL unsteady aerodynamics experiment in the NASA-Ames wind tunnel: a comparison of predictions to measurements, Tech. rep., National Renewable Energy Lab.(NREL), Golden, CO (United States), https://doi.org/10.2172/783409, 2001.

Snel, H., Houwink, R., and Bosschers, J.: Sectional prediction of lift coefficients on rotating wind turbine blades in stall, 1994.

Tachos, N., Filios, A., and Margaris, D.: A comparative numerical study of four turbulence models for the prediction of horizontal axis wind turbine flow, Proceedings of the Institution of Mechanical Engineers, Part C: Journal of Mechanical Engineering Science, 224, 1973–1979, https://doi.org/10.1243/09544062JMES1901, 2010.

Xu, B., Shen, X., Zhang, D., and Chen, J.: Blade optimization for hydrodynamic performance improvement of a horizontal axis tidal current turbine, Ocean Engineering, 290, 116 366, https://doi.org/10.1016/j.oceaneng.2023.116366, 2023a.

Xu, J., Wang, L., Yuan, J., Shi, J., Wang, Z., Zhang, B., Luo, Z., and Tan, A. C.: A cost-effective CNN-BEM coupling framework for design optimization of horizontal axis tidal turbine blades, Energy, 282, 128 707, https://doi.org/10.1016/j.energy.2023.128707, 2023b.

Yang, H., Shen, W., Xu, H., Hong, Z., and Liu, C.: Prediction of the wind turbine performance by using BEM with airfoil data extracted from CFD, Renewable Energy, 70, 107–115, https://doi.org/10.1016/j.renene.2014.05.002, 2014.

Zhang, Z., Yang, Y., Qin, Z., Bashir, M., Cao, Y., Yu, J., Liu, Q., Li, C., and Li, S.: Investigation of dynamic stall models on the aeroelastic responses of a floating offshore wind turbine, Renewable Energy, 237, 121 778, https://doi.org/10.1016/j.renene.2024.121778, 2024.